# Femtosecond polarization-structured optical field meets an anisotropic nonlinear medium

DAN WANG,[1] GUI-GENG LIU,[1] JIA-QI LÜ,[1] PING-PING LI,[1] MENG-QIANG CAI,[1] GUAN-LIN ZHANG,[1] YONGNAN LI,[1] CHENGHOU TU,[1,4] AND HUI-TIAN WANG[2,3,*]

[1]*School of Physics and MOE Key Laboratory of Weak-Light Nonlinear Photonics, Nankai University, Tianjin 300071, China*
[2]*National Laboratory of Solid State Microstructures and School of Physics, Nanjing University, Nanjing 210093, China*
[3]*Collaborative Innovation Center of Advanced Microstructures, Nanjing 210093, China*
[4]*tuchenghou@nankai.edu.cn*
[*]*htwang@nju.edu.cn*

**Abstract:** Filamentation, as a universal femtosecond phenomenon that could occur in various nonlinear systems, has aroused extensive interest, owing to its underlying physics, complexity and applicability. It is always anticipated to realize the controllable and designable filamentation. For this aim, the crucial problem is how to actively break the symmetry of light-matter nonlinear interaction. A kind of extensively used approaches is based on the controllable spatial structure of optical fields involving phase, amplitude and polarization. Here we present an idea to control the optical field collapse by introducing optical anisotropy of matter as an additional degree of freedom, associated with polarization structure. Our theoretical prediction and experimental results reveal that the synergy of optical anisotropy and polarization structure is indeed a very effective means for controlling the optical field collapse, which has the robust feature against random noise.

## References and links

1. P. A. Robinson, "Nonlinear wave collapse and strong turbulence," Rev. Mod. Phys. **69**, 507–573 (1997).
2. L. Bergé, "Wave collapse in physics: principles and applications to light and plasma waves," Phys. Rep. **303**, 259–370 (1998).
3. G. Fibich and B. Ilan, "Vectorial and random effects in self-focusing and in multiple filamentation," Physica D **157**, 112–146 (2001).
4. A. Couairon and A. Mysyrowicz, "Femtosecond filamentation in transparent media," Phys. Rep. **441**, 47–189 (2007).
5. L. Bergé, S. Skupin, R. Nuter, J. Kasparian, and J. P. Wolf, "Ultrashort filaments of light in weakly ionized, optically transparent media," Rep. Prog. Phys. **70**, 1633–1713 (2007).
6. S. A. Akhmanov, A. P. Sukhorukov, and R. V. Khokhlov, "Self-focusing and self-trapping of intense light beams in a nonlinear medium," Sov. Phys. JETP **23**, 1025–1033 (1966).
7. J. M. Soto-Crespo, E. M. Wright, and N. N. Akhmediev, "Recurrence and azimuthal-symmetry breaking of a cylindrical Gaussian beam in a saturable self-focusing medium," Phys. Rev. A **45**, 3168–3175 (1992).
8. L. Bergé, C. Gouédard, J. Schjødt-Eriksen, and H. Ward, "Filamentation patterns in Kerr media vs. beam shape robustness, nonlinear saturation and polarization states," Physica D **176**, 181–211 (2003).
9. A. Vincotte and L. Bergé, "Atmospheric propagation of gradient-shaped and spinning femtosecond light pulses," Physica D **223**, 163–173 (2006).
10. A. Dubietis, G. Tamošauskas, G. Fibich, and B. Ilan, "Multiple filamentation induced by input-beam ellipticity," Opt. Lett. **29**, 1126–1128 (2004).
11. T. D. Grow and A. L. Gaeta, "Dependence of multiple filamentation on beam ellipticity," Opt. Express **13**, 4594–4599 (2005).
12. T. Pfeifer, L. Gallmann, M. J. Abel, D. M. Neumark, and S. R. Leone, "Circular phase mask for control and stabilization of single optical filaments," Opt. Lett. **31**, 2326–2328 (2006).
13. D. W. Li, T. T. Xi, L. Z. Zhang, H. Y. Tao, X. Gao, J. Q. Lin, and Z. Q. Hao, "Interference-induced filament array in fused silica," Opt. Express **25**, 23910–23919 (2017).

14. Z. Q. Hao, K. Stelmaszczyk, P. Rohwetter, W. M. Nakaema, and L. Woeste, "Femtosecond laser filament-fringes in fused silica," Opt. Express **19**, 7799–7806 (2011).
15. V. P. Kandidov, N. Akozbek, M. Scalora, O. G. Kosareva, A. V. Nyakk, Q. Luo, S. A. Hosseini, and S. L. Chin, "Towards a control of multiple filamentation by spatial regularization of a high-power femtosecond laser pulse," Appl. Phys. B **80**, 267–275 (2005).
16. S. M. Li, Y. N. Li, X. L. Wang, L. J. Kong, K. Lou, C. H. Tu, Y. J. Tian, and H. T. Wang, "Taming the collapse of optical fields," Sci. Rep. **2**, 1007 (2012).
17. S. M. Li, Z. C. Ren, L. J. Kong, S. X. Qian, C. H. Tu, Y. N. Li, and H. T. Wang, "Unveiling stability of multiple filamentation caused by axial symmetry breaking of polarization," Photon. Res. **4**, B29–B34 (2016).
18. J. Kasparian and J. P. Wolf, "Physics and applications of atmospheric nonlinear optics and filamentation," Opt. Express **16**, 466–493 (2008).
19. J. Kasparian, M. Rodriguez, G. Méjean, J. Yu, E. Salmon, H. Wille, R. Bourayou, S. Frey, Y. B. André, A. Mysyrowicz, R. Sauerbrey, J. P. Wolf, and L. Wöste, "White-light filaments for atmospheric analysis," Science **301**, 61–64 (2003).
20. A. Camino, Z. Hao, X. Liu, and J. Lin, "High spectral power femtosecond supercontinuum source by use of microlens array," Opt. Lett. **39**, 747750 (2014).
21. R. R. Alfano and S. L. Shapiro, "Emission in the region 4000 to 7000 Å via four-photon coupling in glass," Phys. Rev. Appl. **24**, 584–587 (1970).
22. C. P. Hauri, W. Kornelis, F. W. Helbing, A. Heinrich, A. Couairon, A. Mysyrowicz, J. Biegert, and U. Keller, "Generation of intense, carrier-envelope phase-locked few-cycle laser pulses through filamentation," Appl. Phys. B **79**, 673–677 (2004).
23. H. B. Zhang, Z. J. Yuan, R. Ye, B. He, Y. F. Qi, and J. Zhou, "Filamentation-induced bulk modification in fused silica by excimer laser," Opt. Mater. Express **7**, 3680–3690 (2017).
24. F. Belgiorno, S. L. Cacciatori, M. Clerici, V. Gorini, G. Ortenzi, L. Rizzi, E. Rubino, V. G. Sala, and D. Faccio, "Hawking radiation from ultrashort laser pulse filaments," Phys. Rev. Lett. **105**, 203901 (2010).
25. G. Fibich and B. Ilan, "Deterministic vectorial effects lead to multiple filamentation," Opt. Lett. **26**, 840–842 (2001).
26. Q. Zhan, "Cylindrical vector beams: from mathematical concepts to applications," Adv. Opt. Photon. **1**, 1–57 (2009).
27. X. L. Wang, J. P. Ding, W. J. Ni, C. S. Guo, and H. T. Wang, "Generation of arbitrary vector beams with a spatial light modulator and a common path interferometric arrangement," Opt. Lett. **32**, 3549–3551 (2007).
28. X. L. Wang, Y. N. Li, J. Chen, C. S. Guo, J. P. Ding, and H. T. Wang, "A new type of vector fields with hybrid states of polarization," Opt. Express **18**, 10786–10795 (2010).
29. A. A. Ishaaya, L. T. Vuong, T. D. Grow, and A. L. Gaeta, "Self-focusing dynamics of polarization vortices in kerr media," Opt. Lett. **33**, 13–15 (2008).
30. L. T. Vuong, T. D. Grow, A. A. Ishaaya, A. L. Gaeta, G. W. 't Hooft, E. R. Eliel, and G. Fibich, "Collapse of optical vortices," Phys. Rev. Lett. **96**, 133901 (2006).
31. M. Born and E. Wolf, *Principles of Optics* (Cambridge University, 1999).
32. G. Fibich and A. L. Gaeta, "Critical power for self-focusing in bulk media and in hollow waveguides," Opt. Lett. **25**, 335–337 (2000).
33. A. S. Arabanian and R. Massudi, "Modeling of femtosecond pulse propagation inside $x$-cut and $z$-cut MgO doped LiNbO$_3$ anisotropic crystals," Appl. Opt. **52**, 4212–4222 (2013).
34. http://www.fabrinet.co.th/custappl/casix/aa/product/ prod_cry_ linbo3.html.
35. D. Hovhannisyan and K. Stepanyan, "Femtosecond laser pulse propagation in a uniaxial crystal," J. Mod. Opt. **50**, 2201–2211 (2003).
36. G. Agrawal, *Nonlinear fiber optics* (Academic, 2012).
37. R. P. Chen, L. X. Zhong, K. H. Chew, T. Y. Zhao, and X. Zhang, "Collapse dynamics of a vector vortex optical field with inhomogeneous states of polarization," Laser Phys. **25**, 075401 (2015).

## 1. Introduction

A femtosecond (fs) optical field may undergo the collapse in a transparent Kerr medium [1–6]. As the collapse exacerbates, the higher-order nonlinearity will take over, which will collaborate with the intrinsic diffraction of optical field to counterbalance the self-focusing, resulting ultimately in filamentation [1–17]. In general, the field collapse and subsequent filaments originate from the Kerr-induced modulational instability [1–6]. And the filamentation patterns are initiated by random noise of the optical field itself, which is difficult for us to precisely control and predict them [7–9]. However, it is always anticipated for the realization of controllable field collapse and subsequent filamentation, due to its practical implication [18–24]. For this aim, a great challenge is how to actively control the symmetry breaking of light-matter nonlinear interaction and further to suppress the inherent randomicity of the optical field itself. So far, the widely used methods are to manipulate the spatial structure of scalar optical fields in phase and amplitude [10–15].

Polarization, as intrinsic vectorial nature of light, plays an indispensable role in the light-matter

interaction. However, the spatial diversity of polarization has not yet been adequately utilized in the optical field collapse and subsequent filamentation, only a few of works were related to the control of polarization [16, 17, 25]. We successfully realized the controllable and robust optical field collapse and filamentation via the hybrid polarization structure in an isotropic Kerr medium [16, 17], in which the symmetry of light-matter nonlinear interaction is actively broken by the designable hybrid polarization structure of vector optical fields (VOFs) [26–28] because the induced refractive index change depends on the polarization states. Clearly, polarization, as a manipulable degree of freedom in spatial domain, indeed provides an opportunity and feasibility for controlling the optical field collapse and subsequent filamentation.

To the best of our knowledge, the controllable field collapse and subsequent filamentation mentioned above focus almost on the isotropic nonlinear media. An interesting question is what happens when the polarization-structured VOF meets an optically anisotropic medium. This is just our motivation in this paper, we present an idea for controlling the optical field collapse and subsequent filamentation, based on the synergy of optical anisotropy and spatial polarization structure. We demonstrate the feasibility of our idea by azimuthally-variant linearly-polarized VOFs (AV-LP-VOFs) in optically anisotropic media. Our idea has the robust feature against random noise and opens up a new avenues for controlling the optical field collapse with the aid of optical anisotropy.

## 2. General principle

For the field collapse, the symmetry breaking of light-matter nonlinear interaction requires the existence of self-focusing nucleation(s), where the induced refractive index change $\Delta n$ must be local maximum that requires: (i) $\partial \Delta n/\partial p = \partial \Delta n/\partial q = 0$ and (ii) $\{\partial^2 \Delta n/\partial p^2 < 0\} \cap \{\partial^2 \Delta n/\partial q^2 < 0\}$ (where $p$ and $q$ indicate two orthogonal coordinates in the cross-section of optical field). As is well known, the induced refractive index change $\Delta n$ is directly proportional to the local light intensity $I$ and nonlinear index intensity coefficient $n^I$ (which is proportional to the nonlinear index coefficient $n_2$ or the third-order susceptibility of the nonlinear medium), hence the above conditions become into (i) $\partial I/\partial p = \partial I/\partial q = 0$ and (ii) $\{\partial^2 I/\partial p^2 < 0\} \cap \{\partial^2 I/\partial q^2 < 0\}$ when the third-order susceptibility is space-invariant.

To produce the field collapse and even subsequent filamentation, the optical field should be confined in two transverse dimensions simultaneously. For a cylindrical optical field with a phase or polarization singularity, the focal field has been confined in the radial dimension ($\rho$) due to its donut-shaped focal profile (i.e. $\partial I/\partial \rho|_{\rho=\rho_0} = 0$ and $\partial^2 I/\partial \rho^2|_{\rho=\rho_0} < 0$, where $\rho_0$ is the radius of the strongest ring of the donut-shaped focal field). Thus, whether such a focal field can produce the field collapse and subsequent filamentation, depends only on the induced refractive index change in the azimuthal dimension ($\phi$). In an isotropic medium, we have $\partial I/\partial \phi \equiv 0$ and $\partial^2 I/\partial \phi \equiv 0$ at any azimuthal location for the ideal radially-polarized VOF (RP-VOF), azimuthally-polarized VOF (AP-VOF), and optical vortex field, i.e. they can never collapse and then to produce the filamentation. The field collapsing patterns and subsequent filamentation are unpredictable and uncertain for the practical RP-VOF and AP-VOF [29] and the practical vortex fields [30] in an isotropic medium, because the initial self-focusing nucleations are dominated by random noise. In contrast, for the azimuthally-variant hybridly-polarized VOFs (AV-HP-VOFs) in an isotropic Kerr medium, we have confirmed $\partial \Delta n/\partial \phi = 0$ and $\partial^2 \Delta n/\partial \phi < 0$ at some special azimuthal locations whose polarizations are local linearly polarized [with the maximum $n^I$], this is the reason why AV-HP-VOFs can converge to the deterministic filaments [16, 17].

We anticipate our idea to be able to realize the control on the field collapse and subsequent filamentation, by introducing the optical anisotropy. As is well known, only two orthogonally linearly polarized eigenmodes with different refractive indices are permitted to propagate in an anisotropic medium [31]. In a uniaxial crystal, the two eigenmodes are classified into an *ordinary*-polarized (*o*-polarized) light with an *ordinary* refractive index independent of the

propagation direction and an *extraordinary*-polarized (*e*-polarized) light with an *extraordinary* refractive index depending on the propagation direction. The anisotropy of a uniaxial crystal can be characterized by two principal refractive indices: an *ordinary* index ($n_o$) and an *extraordinary* index ($n_e$). One should be pointed out that the optical anisotropy can be just embodied only by the light-matter interaction.

## 3. Simulations

Here we select a MgO-doped LiNbO$_3$ (MgO:LiNbO$_3$) crystal as an anisotropic medium, which is a negative uniaxial crystal ($n_o > n_e$) belonging to a trigonal (3m) crystal system. The use of MgO:LiNbO$_3$ is to eliminate the refractive index change caused by the photorefractive effect. For any uniaxial crystal, the *x* and *y* axes are optically equivalent, while a unique distinguishable direction is the *z* axis called the optic axis. As is well known, when an optical field propagates along the *z* axis, both *x*- and *y*-polarized components are the ordinary light with the same refractive index of $n_o$, similar to the propagation of light in an isotropic medium [31]. That is to say, in this case the anisotropy cannot be reflected, of course, the anisotropy cannot also be utilized. As the best choice, therefore, the optical field should enter into the MgO:LiNbO$_3$ crystal along the *x* (or *y*) axis, implying that the *y*- (or *x*-) and *z*-polarized components are the *o*- and *e*-polarized light with the respective refractive indices of $n_o$ and $n_e$, as shown in Fig. 1.
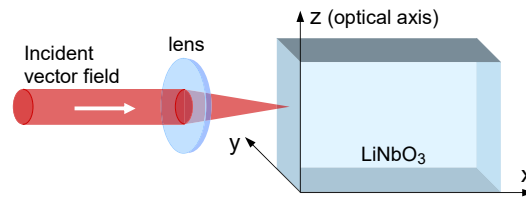


Fig. 1. Schematic of configuration for investigating the collapse of VOFs in an anisotropic MgO:LiNbO$_3$ crystal.

In this schematic, we have omitted the generation unit of fs AV-LP-VOFs. The generated AV-LP-VOFs have a central wavelength of 800 nm, a single pulse energy of 6.0 μJ, a pulse duration of ~65 fs, and a "top-hat-like" profile (excluding a central singularity caused by polarization uncertainty) with a radius of 1.5 mm. The focused AV-LP-VOF, by an achromatic lens with a focal length of 100 mm, is normally incident on the *x*-cut MgO:LiNbO$_3$ with a length of 20 mm. The intensity pattern of the field transmitted from MgO:LiNbO$_3$ is imaged on a detector (Beamview, Coherent Inc.) by another achromatic lens with a focal length of 200 mm.

Under the weak focusing situation, the focused AV-LP-VOF exhibits a uniform-intensity focal ring instead of a focal spot. In the polar coordinate system ($r, \phi$), it can be written as

$$\mathbf{E}(r, \phi) = A(r)(\cos \delta \hat{\mathbf{e}}_y + \sin \delta \hat{\mathbf{e}}_z). \tag{1}$$

Here $A(r)$ represents the radially-variant amplitude and can be described by a generalized hypergeometric function. As a well approximation, $A(r)$ can be taken as a form of $A(r) = a_0 r \exp(-r^2/2r_0^2)$, where $r_0$ is the radius of the focal ring. $\delta = m\phi + \delta_0$ (*m* is the topological charge and $\delta_0$ is the initial phase). $\hat{\mathbf{e}}_y$ and $\hat{\mathbf{e}}_z$ are a pair of orthogonal unit vectors in the *y*- and *z*-axes shown in Fig. 1, and indicate the polarization directions of the *o*- and *e*-polarized components, respectively. For AV-LP-VOF with *m* and $\delta_0$, the local *o*- and *e*-polarized components in the *yz* plane should locate at a series of azimuthal locations $\phi_o(n) = n\pi/m - \delta_0/m$ and $\phi_e(n) = (2n + 1)\pi/2m - \delta_0/m$ (where $n = 0, 1, ..., 2m - 1$), respectively.

To theoretically explore the nonlinear propagation behavior of a VOF in the *x*-cut MgO:LiNbO$_3$, the (2+1)-dimensional vector-version nonlinear-Schrödinger equation (NLSE) should be used.

Under the slowly varying amplitude approximation, the vector-version NLSE can be divided into a pair of coupled NLSEs for the $o$- and $e$-polarized components

$$\frac{\partial \psi_o}{\partial \zeta} = j\nabla_\perp^2 \psi_o + j\frac{4\alpha P}{P_o^C}\left[|\psi_o|^2\psi_o + \frac{\chi_{16}}{\chi_{11}}\left(2|\psi_e|^2\psi_o + \psi_e^2\psi_o^*\right)\right], \tag{2a}$$

$$\frac{\partial \psi_e}{\partial \zeta} = j\frac{n_o^0}{n_e^0}\nabla_\perp^2 \psi_e + j\frac{4\alpha P}{P_e^C}\left[|\psi_e|^2\psi_e + \frac{\chi_{16}}{\chi_{33}}\left(2|\psi_o|^2\psi_e + \psi_o^2\psi_e^*\right)\right], \tag{2b}$$

where $\psi_o$ ($\psi_e$) is the dimensionless $o$-polarized ($e$-polarized) component normalized by the total field, $\psi_{o,e}(\rho, \phi; \zeta) = E_{o,e}(\rho, \phi; \zeta)/\sqrt{\iint[|E_o(\rho, \phi; \zeta)|^2 + |E_e(\rho, \phi; \zeta)|^2]\rho d\rho d\phi}$. $\rho = r/r_0$ and $\zeta = x\lambda/4\pi n_o^0 r_0^2$ are the dimensionless cylindrical coordinates, and $P = 2n_o^0\varepsilon_0 c \iint[|E_o(\rho, \phi; \zeta)|^2 + |E_e(\rho, \phi; \zeta)|^2]\rho d\rho d\phi$ is the input power. $P_o^C = \alpha\lambda^2/4\pi n_o^0 n_o^I$ and $P_e^C = \alpha\lambda^2/4\pi n_e^0 n_e^I$ are the critical powers for self-focusing, which are related to the $o$- and $e$-polarized components, respectively. $n_o^0$ ($n_e^0$) and $n_o^I = 3\chi_{11}/4(n_o^0)^2\varepsilon_0 c$ ($n_e^I = 3\chi_{33}/4(n_e^0)^2\varepsilon_0 c$) are the linear refractive index and the nonlinear refractive coefficient of the $o$-polarized ($e$-polarized) component in the uniaxial crystal, respectively. $\alpha$ is in general a constant dependent on the initial field shape [32]. $\varepsilon_0$, $c$ and $\lambda$ are the permittivity, the speed of light and the wavelength, in the free space, respectively. On the right-hand side of Eq. (2), the first term is the contribution from the diffraction effect described by the transverse Laplacian $\nabla_\perp^2 = \partial^2/\partial\rho^2 + \frac{1}{\rho}\partial/\partial\rho + \frac{1}{\rho^2}\partial^2/\partial\phi^2$ and the second term is attributed to the contribution of the Kerr nonlinearity, respectively. It should be pointed out that we only concentrate on the collapsing behavior, thus the higher-order nonlinearity has been neglected.

MgO:LiNbO$_3$ has the physical parameters: the ordinary and extraordinary linear refractive indices of $n_o^0 = 2.24717$ and $n_e^0 = 2.16539$ at $\lambda = 800$ nm with the Sellmeier equations [33, 34], the nonlinear susceptibilities of $\chi_{11} = 9.79523 \times 10^{-16}$ cm$^2$/W, $\chi_{33} = 9.79521 \times 10^{-16}$ cm$^2$/W and $\chi_{16} = 2.86026 \times 10^{-16}$ cm$^2$/W [33, 35], respectively. Clearly, MgO:LiNbO$_3$ is a negative uniaxial crystal ($n_o^0 > n_e^0$). For MgO:LiNbO$_3$ belonging to a trigonal ($3m$) symmetry system, one should have $\chi_{11} = \chi_{33}$ in theory, we have indeed $\chi_{11} \simeq \chi_{33}$ from the measured values mentioned above and $P_o^C = NP_e^C = P^C$. Here we must point out that in Eq. (2), $P^C$ is the critical power for a Gaussian mode instead of AV-LP-VOF, and $\alpha$ is also a parameter related to a Gaussian profile and so should be taken $\alpha = 2$ [32].

After introducing two parameters, defined as $N = n_o^0/n_e^0$ and $\beta = \chi_{16}/\chi_{11} = \chi_{16}/\chi_{33}$ for the sake of description or discussion, Eq. (2) can be rewritten as

$$\frac{\partial \psi_o}{\partial \zeta} = j\nabla_\perp^2 \psi_o + j\frac{8P}{P^C}\left[|\psi_o|^2\psi_o + \beta\left(2|\psi_e|^2\psi_o + \psi_e^2\psi_o^*\right)\right], \tag{3a}$$

$$\frac{\partial \psi_e}{\partial \zeta} = jN\nabla_\perp^2 \psi_e + jN\frac{8P}{P^C}\left[|\psi_e|^2\psi_e + \beta\left(2|\psi_o|^2\psi_e + \psi_o^2\psi_e^*\right)\right]. \tag{3b}$$

In fact, $N$ and $\beta$ are used to classify the linear and nonlinear anisotropies, respectively. In detail, $N = 1$ ($N \neq 1$) indicates the linear isotropy (anisotropy); $\beta = 1/3$ ($\beta \neq 1/3$) corresponds to the nonlinear isotropy (anisotropy).

All the simulations are carried out based on Beam Propagation Method [36], which is used to numerically solve Eq. (2) or Eq. (3) to model the collapsing behavior of AV-LP-VOFs in the anisotropic MgO:LiNbO$_3$. Differently from the conventional isotropic Kerr medium, to clarify the contributions of both linear and nonlinear anisotropies to the collapsing behaviors of AV-LP-VOFs in the anisotropic nonlinear crystal, we perform the detailed simulations (see Appendix). After summarizing all the simulation results, we get the following conclusions.

(i) In the media with linear isotropy ($n_o = n_e$) and nonlinear anisotropy, when $\beta < 1/3$, AV-LP-VOF with $m$ and $\delta_0$ will collapse into $4m$ deterministic filaments exhibiting the $C_{4m}$ rotation symmetry, located at the azimuthal locations of $\phi(n) = n\pi/2m - \delta_0/m$ (where $n = 0, 1, ..., 4m-1$);

when $\beta > 1/3$ corresponding to the $BaF_2$ crystal, AV-LP-VOF with $m$ and $\delta_0$ will collapse into $4m$ deterministic filaments exhibiting the $C_{4m}$ rotation symmetry, located at the azimuthal locations of $\phi(n) = (2n + 1)\pi/4m - \delta_0/m$ (where $n = 0, 1, ..., 4m - 1$).

(ii) In the media with both linear and nonlinear anisotropies, when $\beta < 1/3$ corresponding to the $x$-cut MgO:LiNbO$_3$ crystal, AV-LP-VOF with $m$ and $\delta_0$ will collapse into $2m$ deterministic filaments located at the azimuthal locations of $\phi(n) = n\pi/m - \delta_0/m$ (where $n = 0, 1, ..., 2m - 1$); when $\beta > 1/3$, AV-LP-VOF with $m$ and $\delta_0$ will collapse into $4m$ deterministic filaments exhibiting the $C_{4m}$ rotation symmetry, located at the azimuthal locations of $\phi(n) = (2n + 1)\pi/4m - \delta_0/m$ (where $n = 0, 1, ..., 4m - 1$).

(iii) For all the above cases, the appearance of filamentation requires that: the locations of filaments must satisfy the two conditions where the local linear polarization is remained and the ellipticity has a negative slope, however, which are necessary but not sufficient. One should be pointed out that at the locations of filaments, the polarization states of light correspond to the $o$-polarization in the negative uniaxial crystal.

## 4.  Experiments

Firstly, we focus on the collapsing behaviors of AV-LP-VOFs ($m = 1$ and 2) for three different initial phases ($\delta_0 = 0, \pi/4$ and $\pi/2$), as shown in Fig. 2. One should be pointed out that for two particular cases of $(m, \delta_0) = (1, 0)$ and $(m, \delta_0) = (1, \pi/2)$, AV-LP-VOFs described by Eq. (1) are RP-VOFs and AP-VOFs, respectively. Any AV-LP-VOF has a uniform intensity pattern excluding a central polarization singularity (first row). When a horizontal polarizer is used, implying that the allowed polarized component corresponds to the $o$-polarized component in the MgO:LiNbO$_3$
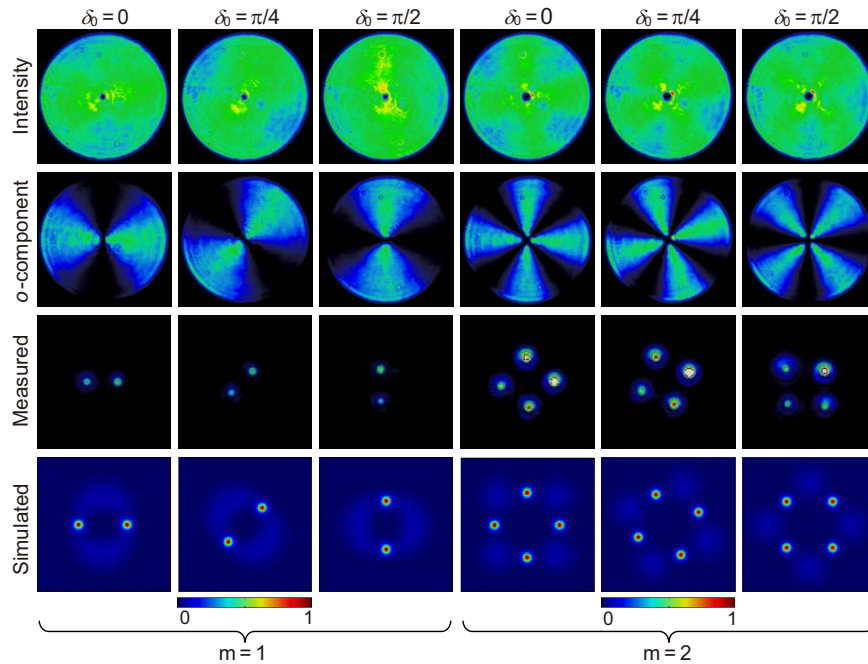


Fig. 2. The collapsing behaviors of AV-LP-VOFs ($m = 1$ and 2) for three different initial phases ($\delta_0 = 0, \pi/4$ and $\pi/2$). Measured patterns of total intensity and $o$-polarized component of the created vector fields in the $x$-cut MgO:LiNbO$_3$ crystal are shown in the first and second rows. The third and fourth rows correspond to the measured and simulated collapsing patterns, respectively.

crystal, all AV-LP-VOFs exhibit the fan-like extinction intensity patterns with $2m$ fan-like regimes (second row). After the focused AV-LP-VOFs with $m = 1$ and 2 interact with the anisotropic MgO:LiNbO$_3$ crystal, respectively, the measured results of the produced collapsing patterns in the third row are in good agreement with the simulated ones in the fourth row. Clearly, the number of filaments is $2m$ depending only on $m$. The collapsing field pattern for $m = 1$ is rotated counterclockwise with a step of $\pi/4$ as $\delta_0$ increases from $\delta_0 = 0$ to $\delta_0 = \pi/4$ and $\pi/2$ (third and fourth rows). The collapsing field pattern for $m = 2$ is also rotated counterclockwise with a step of $\pi/8$ as $\delta_0$ increases from $\delta_0 = 0$ to $\delta_0 = \pi/4$ and $\pi/2$ (third and fourth rows). In particular, the filaments always occur at a series of azimuthal locations, where the polarizations of optical field are $o$-polarized in the LiNbO$_3$ crystal.

   Secondly, we investigate the collapsing behaviors of the focused AV-LP-VOFs with higher topological charges. As examples, Fig. 3 shows the measured and simulated results of the collapsed AV-LP-VOFs with $m = 3, 4, 5, 6$ for $\delta_0 = 0$ and $\pi/2$. These AV-LP-VOFs also have uniform intensity patterns excluding a central polarization singularity (not shown). The $o$-polarized components of the initial AV-LP-VOFs exhibit fan-like extinction patterns with $2m$-fold rotation symmetry (the first and fourth columns). The measured collapsing patterns of the focused AV-LP-VOFs in the second (fifth) column are in good agreement with the simulated ones in the third (sixth) column. Clearly, the focused AV-LP-VOFs with $m$ (= 3, 4, 5, 6) produce $2m$ (= 6, 8, 10, 12) deterministic filaments, respectively, for either $\delta_0 = 0$ or $\delta_0 = \pi/2$. The collapsing pattern exhibits a $2m$-fold rotation ($C_{2m}$) symmetry. The simulated and measured results demonstrate again the fact that the filaments are always located at the azimuthal locations, where the polarizations of
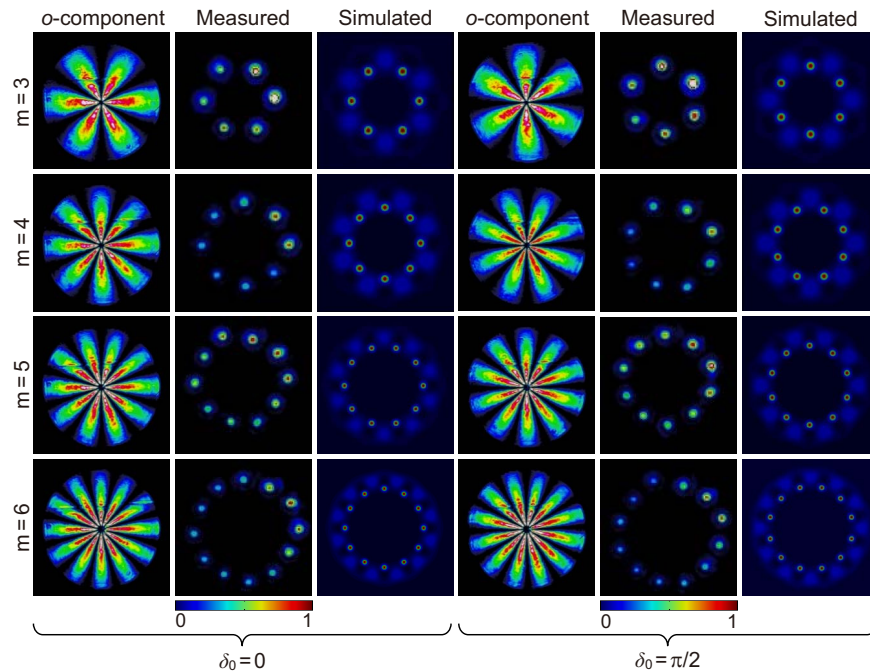


Fig. 3. The collapsing behaviors of AV-LP-VOFs ($m = 3, 4, 5, 6$) for two different initial phases ($\delta_0 = 0, \pi/2$). The first three columns correspond to four AV-LP-VOFs ($m = 3, 4, 5, 6$) with $\delta_0 = 0$, while the last three columns correspond to four AV-LP-VOFs ($m = 3, 4, 5, 6$) with $\delta_0 = \pi/2$. Measured patterns of $o$-polarized component of the created AV-LP-VOFs in the uniaxial crystal are shown in the first and fourth columns. The second (fifth) and third (sixth) columns correspond to the measured and simulated collapsing patterns, respectively.

AV-LP-VOFs are $o$-polarized.

Thirdly, all the above filamentation only takes place in the $x$-cut MgO:LiNbO$_3$ crystal whose optic axis is directed vertically, as shown in Fig. 1. To explore the relationship between the collapsing pattern of AV-LP-VOF and the orientation of the $x$-cut MgO:LiNbO$_3$ crystal, we can change the angle $\theta$ between the vertical direction and the optic axis ($z$ axis) of the crystal by rotating the $x$-cut MgO:LiNbO$_3$ crystal around its $x$ axis. As shown in Fig. 1, the optical axis ($z$ axis) is directed vertically, which is defined as $\theta = 0°$. As two examples, Figs. 4(a) and 4(b) show the evolutions of the measured collapsing patterns of RP-VOF ($m = 1$, $\delta_0 = 0$) and AV-LP-VOF ($m = 2$, $\delta_0 = 0$) with $\theta$, respectively. When $\theta$ is changed from $\theta = 0°$ to $\theta = 180°$ by a step of $10°$, the collapsing patterns are rotated counterclockwise in sequence by an angle of $10°/m$ and the collapsing location always corresponds the ordinary polarization in the uniaxial crystal in each case.
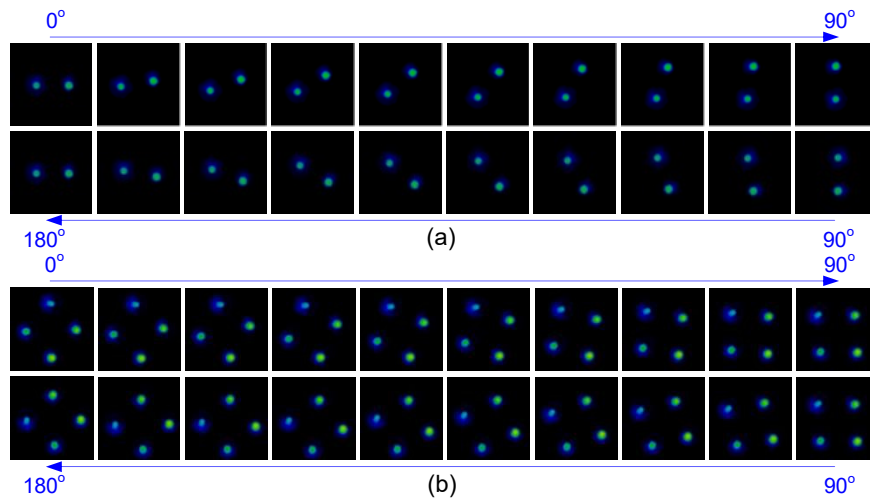


Fig. 4. The relationship between the collapsing patterns of AV-LP-VFs and the orientation of the crystal. The collapsing patterns of RP-VOF ($m = 1$, $\delta_0 = 0$) and AV-LP-VOF ($m = 2$, $\delta_0 = 0$) rotated with the optic axis of the MgO:LiNbO$_3$ crystal are shown in Figs. 4(a) and 4(b), respectively.

Summarizing all the above experimental results, we get the following conclusions. For a AV-LP-VOF with a given $m$, its focused field is normally incident into an $x$-cut uniaxial MgO:LiNbO$_3$: (i) the anisotropy of nonlinear media can result in the axial-symmetry breaking of the nonlinear interaction; (ii) AV-LP-VOF undergoes the collapse to converge into the $2m$ deterministic filaments depending solely on $m$; (iii) the collapsing pattern exhibits a $2m$-fold rotation ($C_{2m}$) symmetry; (iv) the filaments are always located at the azimuthal locations $\phi_o(n)$, where the local polarizations correspond to the ordinary polarization in the uniaxial crystal. These experimental results are in well agreement with the simulation results described in Section 3 and Appendix as follows: In the $x$-cut MgO:LiNbO$_3$ crystal ($\beta < 1/3$), AV-LP-VOF with $m$ and $\delta_0$ will collapse into $2m$ deterministic filaments located at the azimuthal locations of $\phi(n) = n\pi/m - \delta_0/m$ (where $n = 0, 1, ..., 2m - 1$) and the polarization states at the locations of filaments correspond to the $o$-polarization in the negative uniaxial crystal.

## 5. Discussion

The simulation results in Appendix also show that collapsing behaviors of AV-LP-VOF with $m$ and $\delta_0$ in the media with linear isotropy ($N = 1$) and nonlinear anisotropy ($\beta < 1/3$ and

$\beta > 1/3$). To confirm our simulation results in experiment, we find a nonlinear medium, $BaF_2$, which is a crystal to have the linear isotropy but the nonlinear anisotropy ($\beta > 1/3$). Figure 5 shows the collapsing patterns of AV-LP-VOF with $m = 1$ but different $\delta_0 = 0$, $\pi/4$, $\pi/2$ and $3\pi/2$ in $BaF_2$ under the lower input power. Clearly, the measured patterns are in good agreement with the simulated ones in $BaF_2$, as conclusions summarized in Appendix, AV-LP-VOF with $m$ and $\delta_0$ will collapse into $4m$ deterministic filaments, located at the azimuthal locations of $\phi(n) = (2n+1)\pi/4m - \delta_0/m$ (where $n = 0, 1, \ldots, 4m-1$), in the medium with the linear isotropy but nonlinear anisotropy ($\beta > 1/3$).
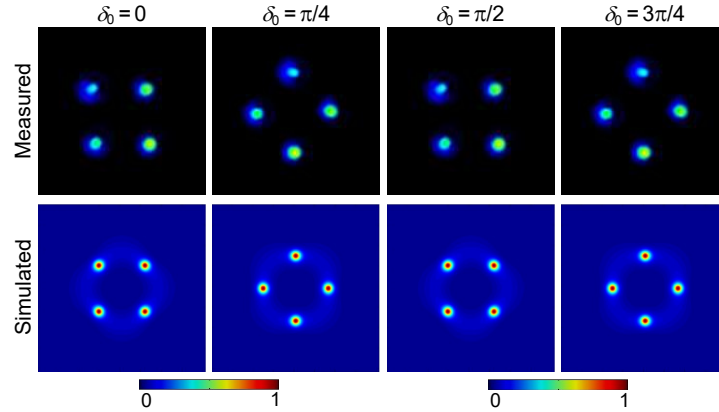


Fig. 5. Measured and simulated collapsing behaviors of AV-LP-VFs with $m = 1$ but with different $\delta_0 = 0, \pi/4, \pi/2$ and $3\pi/2$ in $BaF_2$ with the linear isotropy but nonlinear anisotropy ($\beta > 1/3$).

Although the simulation can give the collapsing behaviors of AV-LP-VOF in various nonlinear media, the physics behind the multiple filamentation has still no clear picture. To clearly understand the physics behind the collapse of AV-LP-VOF, it will be very beneficial and valuable to apply both the non-depletion approximation theroy and the azimuthal modulational instability (AMI) theroy to Eq. (3). Multiple filamentation requires the simultaneous spatial confinements in both the radial and azimuthal dimensions. The self-confinement in the radial dimension is due to the focal ring. However, it is of great interest and of crucial importance to reveal the mechanism behind the axial symmetry breaking that leads to the multiple filamentation. Therefore, we ignore the radial terms $\partial^2/\partial\rho^2$ and $\partial/\partial\rho$ in the transverse Laplacian $\nabla_\perp^2$, while concentrate only on the azimuthal term $\partial^2/\partial\phi^2$ in Eq. (3).

## 5.1. Non-depletion approximation analysis

The Kerr medium is divided into $M$ equal-length thin segments (each thin segment has a normalized length of $Z = L/M$), so that the non-depletion approximation is valid within any thin segment. After the focused AV-LP-VOF described in Eq. (3) passing though the 1st segment of the anisotropic nonlinear medium, based on Eq. (3), the increases of $\psi_0$ and $\psi_e$ should be

$$\Delta\psi_o = -j\left[m^2 - B\left(\cos^2\delta + 3\beta\sin^2\delta\right)\right] Z\cos\delta, \tag{4a}$$

$$\Delta\psi_e = -jN\left[m^2 - B\left(\sin^2\delta + 3\beta\cos^2\delta\right)\right] Z\sin\delta, \tag{4b}$$

where $B = 8P/P^C$. However, we must point out that $P^C$ is only the critical power under the incidence of Gaussian beam. The critical power $P_m^C$ of AV-LP-VOF with the topological charge $m$ has a connection with $P^C$ as $P_m^C = 6m^2 P^C/5$ [37], so the parameter $B$ for AV-LP-VOF should be

rewritten as $B = 48m^2 P/5P_m^C$. We easily yield the first-order derivative of the intensity increase $\Delta I = |\Delta\psi_o|^2 + |\Delta\psi_e|^2$ to $\phi$ as follows

$$\frac{\partial\Delta I}{\partial\phi} = \frac{1}{6}mZ^2 W\sin(2\delta),$$ (5a)

with

$$W = UV\cos(2\delta) - (N^2 - 1)(U + V\cos^2\delta)V\sin^2\delta,$$ (5b)

$$U = 4m^2 - 3B(1 + \beta) = 4m^2[1 - 36P(1 + \beta)/5P_m^C],$$ (5c)

$$V = 3B(1 - 3\beta).$$ (5d)

We always have $U < 0$ for any $m$, because $P/P_m^C > 1$ is required for the collapsing of AV-LP-VOF.

To determine the azimuthal locations of filamentation, the key is the sign of the second-order derivative of $\Delta I$ to $\phi$, we have

$$\frac{\partial^2\Delta I}{\partial\phi^2} = \frac{1}{6}mZ^2\left[\frac{\partial W}{\partial\phi}\sin(2\delta) + 2mW\cos(2\delta)\right].$$ (6)

We will analytically discuss the collapsing of AV-LP-VOFs in two cases below.

### 5.1.1. In nonlinear media with linear isotropy

We discuss a special case when the nonlinear medium has the linear isotropy ($N = 1$), we have from Eqs. (5) and (6)

$$\frac{\partial\Delta I}{\partial\phi} = \frac{1}{12}mZ^2 UV\sin(4\delta),$$ (7a)

$$\frac{\partial^2\Delta I}{\partial\phi^2} = \frac{1}{3}m^2 Z^2 UV\cos(4\delta).$$ (7b)

We can divide this case into three subcases of (i) $\beta = 1/3$, (ii) $\beta < 1/3$ and (iii) $\beta > 1/3$.

**Subcase–(i)** of $\beta = 1/3$.

This corresponds to the traditional isotropic Kerr nonlinear medium, we always have $\partial\Delta I/\partial\phi \equiv 0$ and $\partial^2\Delta I/\partial\phi^2 \equiv 0$ in Eq. (7), implying that any azimuthal position is equivalent or indistinguishable for any AV-LP-VOF. Therefore, any purely ideal AV-LP-VOF can never produce the deterministic filaments, which is in well agreement with the simulation (first column of Fig. 6 in Appendix) and [29]. Accordingly, the collapsing of a practical AV-LP-VOF originates from the random fluctuation (second column of Fig. 6 and [29]).

**Subcase–(ii)** of $\beta < 1/3$.

We have $V > 0$ and $U < 0$ in Eq. (7). When $\sin(4\delta) = 0$, i.e. $4\delta = 2n\pi$ or $4\delta = (2n + 1)\pi$ (where $n$ is an integer), $\partial\Delta I/\partial\phi = 0$ in Eq. (7a). Clearly, at $\phi(n) = n\pi/2m - \delta_0/m$ (where $n = 0, 1, ..., 4m - 1$), we have $\partial^2\Delta I/\partial\phi^2 < 0$ in Eq. (7b), implying that the filaments of AV-LP-VOF will be produced because their optical intensities are maximum. In contrast, when $4\delta = (2n + 1)\pi$, we have $\partial^2\Delta I/\partial\phi^2 > 0$ in Eq. (7b), implying that at $\phi(n) = (2n + 1)\pi/4m - \delta_0/m$ (where $n = 0, 1, ..., 4m - 1$) the filaments cannot be produced because their optical intensities are minimum. These analytic results are in completely agreement with the simulation results.

**Subcase–(iii)** of $\beta > 1/3$.

This corresponds to the BaF$_2$ crystal, we have $V < 0$ and $U < 0$ in Eq. (7). To make $\partial\Delta I/\partial\phi = 0$ in Eq. (7a), it is required $\sin(4\delta) = 0$, implying that $4\delta = 2n\pi$ or $4\delta = (2n + 1)\pi$ (where $n$ is an integer). Clearly, when $4\delta = 2n\pi$, we have $\partial^2\Delta I/\partial\phi^2 > 0$ in Eq. (7b), implying that at $\phi(n) = n\pi/2m - \delta_0/m$ (where $n = 0, 1, ..., 4m - 1$) the filaments cannot be produced because their

optical intensities are minimum. In contrast, when $4\delta = (2n + 1)\pi$, we have $\partial^2 \Delta I / \partial \phi^2 < 0$ in Eq. (7b), implying that at $\phi(n) = (2n + 1)\pi/4m - \delta_0/m$ (where $n = 0, 1, ..., 4m - 1$) the filaments of AV-LP-VOF will be produced because their optical intensities are maximum, which are in completely agreement with both the experimental results in the BaF$_2$ crystal and the simulation results.

### 5.1.2.   In nonlinear media with both linear and nonlinear anisotropies

We discuss the relatively general case when the nonlinear medium has both linear anisotropy ($N > 1$) and the nonlinear anisotropy $\beta \neq 1/3$. To make $\partial \Delta I / \partial \phi = 0$ in Eq. (5), we require to satisfy Condition-I of $\sin(2\delta) = 0$ or Condition-II of $W = 0$. We can classify into two subcases: Subcase-(i) of $\beta < 1/3$ and Subcase-(ii) of $\beta > 1/3$.

   **Subcase–(i)** of $\beta < 1/3$ corresponding to the MgO:LiNbO$_3$ crystal ($V > 0$, $N > 1$).

   Under the Condition-I of $\sin(2\delta) = 0$ corresponding to $2\delta = n\pi$ (where $n = 0, 1, ..., 4m - 1$), we can confirm $\partial^2 \Delta I / \partial \phi^2 < 0$ at $\phi(n) = n\pi/2m - \delta_0/m$ (see Appendix for the details), implying that there has the possibility of the filamentation for AV-LP-VOF at the $4m$ azimuthal locations because their intensities are local maximum. However, this analytic result agrees with the simulated results for the initial collapse stage (see third and fourth columns of Fig. 8 in Appendix), but has some difference from the experimental and final simulated results (Fig. 2) that the observed final filaments occur at the $2m$ azimuthal locations of $\phi(n) = n\pi/m - \delta_0/m$ (where $n = 0, 1, ..., 2m - 1$), which can be understood below. The two conditions for the filamentation, $\partial \Delta I / \partial \phi = 0$ and $\partial^2 \Delta I / \partial \phi^2 < 0$, are necessary but not sufficient. Without loss of generality, we select RP-VOF as an example. For the linear anisotropy, we consider the negative uniaxial crystal ($N_o^0 > N_e^0$, $N > 1$). The simulated linear propagation behavior of RP-VOF in the negative uniaxial media with ($N > 1$, $\beta = 0$) is very similar to the intensity profile in lower left corner of Fig. 8, which shows the two strong spots at $\phi = 0$ and $\pi$ due to the anisotropic propagation in the anisotropic medium. Thus, among the four possible locations ($\phi = 0$, $\pi/2$, $\pi$ and $3\pi/2$) determined by the above filamentation conditions, only at the two locations ($\phi = 0$ and $\pi$) the filamentation is allowed.

   Under the Condition-II, we can conform that at azimuthal locations determined by $W = 0$, $\partial^2 \Delta I / \partial \phi^2 > 0$ (see Appendix for the details), suggesting that the filaments for the AV-LP-VOF can never be produced because their intensities are minimum.

   **Subcase–(ii)** of $\beta > 1/3$.

   Under the Condition-I of $\sin(2\delta) = 0$ corresponding to $2\delta = n\pi$ (where $n = 0, 1, ..., 4m - 1$), we can confirm $\partial^2 \Delta I / \partial \phi^2 > 0$ at $\phi(n) = n\pi/2m - \delta_0/m$ (see Appendix), meaning that the filaments cannot be produced because their intensities are minimum.

   Under the Condition-II, we can confirm $\partial^2 \Delta I / \partial \phi^2 < 0$ at azimuthal locations determined by $W = 0$ (see Appendix), suggesting that the filaments for AV-LP-VOF can be produced because their intensities are maximum. For the weak linear anisotropy ($N \to 1$), we can have $\cos(2\delta) \approx 0$ from $W = 0$, which is very similar to the linear isotropic case discussed above. Thus at $\phi(n) \approx n\pi/2m + \pi/4m - \delta_0/m$, the filaments can be produced, which agrees with the simulation result shown in Appendix.

### 5.2.   Plane wave analysis

We now will use the plane wave analysis method to deepen the understanding of the filamentation of the AV-LP-VOF propagation in the nonlinear media again. First, we analytically find the steady-state solutions of Eq. (3) using the method described in detail in [7–9]. Then, we apply the azimuthal perturbation to one of the steady-state solutions. Finally, we can find the azimuthal modulational instability (AMI) growth rate $\gamma_m$ (the detailed calculation process has been shown

in Appendix) as

$$\gamma_m^2 = \frac{m^2}{\bar{\rho}^2} \left\{ B \left[ \left(N^2 \cos^2\delta + \sin^2\delta\right) + \sqrt{\left(N^2 \cos^2\delta - \sin^2\delta\right)^2 + N^2(3\beta)^2 \sin^2(2\delta)} \right] - \frac{m^2}{\bar{\rho}^2} \right\},$$

(8)

where $\bar{\rho}$ is the mean radius of the focal field ring.

To determine the azimuthal locations of the filaments, the key is to find the maximum value of $\gamma_m$. With Eq. (8), we will analyze the number and location of filaments in the two cases below.

### 5.2.1. In nonlinear media with linear isotropy

We discuss a special case when the nonlinear medium has the linear isotropy ($N = 1$), Eq. (8) becomes into

$$\gamma_m^2 = \frac{m^2}{\bar{\rho}^2} \left\{ B \left[ 1 + \sqrt{1 + (3\beta + 1)(3\beta - 1)\sin^2(2\delta)} \right] - \frac{m^2}{\bar{\rho}^2} \right\}.$$

(9)

We can divide this case into three subcases of (i) $\beta = 1/3$, (ii) $\beta < 1/3$ and (iii) $\beta > 1/3$.

**Subcase–(i)** of $\beta = 1/3$.

This corresponds to the traditional isotropic Kerr nonlinear medium, we have $\gamma_m^2 = (m^2/\bar{\rho}^2)(2B - m^2/\bar{\rho}^2)$ in Eq. (9), implying that any azimuthal position is equivalent or indistinguishable for any AV-LP-VOF. Therefore, any purely ideal AV-LP-VOF can never produce the deterministic multiple filamentation, which is in excellent agreement with the simulation (first column of Fig. 6 in Appendix) and [29].

**Subcase–(ii)** of $\beta < 1/3$.

In this subcase, when $\sin^2(2\delta) = 0$, $\gamma_m^2$ in Eq. (9) reaches its maximum $(\gamma_m^2)_{max} = (m^2/\bar{\rho}^2)(2B - m^2/\bar{\rho}^2)$. Clearly, the filaments of AV-LP-VOF will be produced at $\phi(n) = n\pi/2m - \delta_0/m$ (where $n = 0, 1, ..., 4m - 1$). These analytic results are in completely agreement with the simulation results and the non-depletion approximation analysis.

**Subcase–(iii)** of $\beta > 1/3$.

This corresponds to the BaF$_2$ crystal. To make $\gamma_m^2$ in Eq. (9) reach its maximum $(\gamma_m^2)_{max} = (m^2/\bar{\rho}^2)[B(1 + 3\beta) - m^2/\bar{\rho}^2]$, it is required $\sin^2(2\delta) = 1$, implying that the filaments of AV-LP-VOF will be produced at $\phi(n) = (2n + 1)\pi/4m - \delta_0/m$ (where $n = 0, 1, ..., 4m - 1$), which are in completely agreement with the experimental results in the BaF$_2$ crystal, the simulation results and the non-depletion approximation analysis.

### 5.2.2. In nonlinear media with both linear and nonlinear anisotropies

We now discuss the relatively general case when the nonlinear medium has both linear anisotropy ($N > 1$) and the nonlinear anisotropy $\beta \neq 1/3$. To determine the azimuthal locations of the filaments, the key is also to find the maximum value of $\gamma_m^2$ in Eq. (8). Figure 9 illustrates the AMI growth rate $\gamma_m^2$ in two subcases: Subcase–(i) of $\beta < 1/3$ and Subcase–(ii) of $\beta > 1/3$.

**Subcase–(i)** of $\beta < 1/3$ corresponding to the MgO:LiNbO$_3$ crystal.

The analytical results of RP-VOF given by Eq. (8) are shown in Fig. 9(c). When $N = 1$, $\beta < 1/3$, $(\gamma_m^2)_{max}$ of RP-VOF are located at the azimuthal locations of $\phi = 0$, $\pi/2$, $\pi$ and $3\pi/2$, which are owing to the nonlinear anisotropy ($\beta < 1/3$). However, when $N > 1$, $\beta < 1/3$, $(\gamma_m^2)_{max}$ of RP-VOF are located at the azimuthal locations of $\phi = 0$ and $\pi$, which originate from the collaborative contribution of the linear and nonlinear anisotropies to the axial-symmetry breaking. Clearly, the symmetry breaking caused by the linear anisotropy ($N > 1$) results in that four $(\gamma_m^2)_{max}$ of RP-VOF in the linear isotropic nonlinear medium become into two $(\gamma_m^2)_{max}$ in the both linear and nonlinear anisotropic medium. In fact, AV-LP-VOF will collapse into $2m$ deterministic filaments located at the azimuthal locations of $\phi(n) = n\pi/m - \delta_0/m$ (where $n = 0, 1, ..., 2m - 1$), which are in completely agreement with both the experimental results in the MgO:LiNbO$_3$ crystal and the simulation results.

**Subcase–(ii)** of $\beta > 1/3$.

The analytical results of RP-VOF given by Eq. (8) are shown in Fig. 9(b). The AMI growth rate $(\gamma_m^2)_{max}$ of RP-VOF will determine four filaments in the media ($N = 1.038$, $\beta > 1/3$), which are approximately located at the azimuthal locations of $\phi \approx \pi/4$, $3\pi/4$, $5\pi/4$, $7\pi/4$, although they look the same as the case ($N = 1$, $\beta > 1/3$). In fact, the locations of filaments depend on the strength of linear anisotropy (the value of $N$), as demonstrated by the analytical result of the case (for lager $N = 1.1$) shown in Fig. 9(b) are in good agreement with the numerical simulation shown in the last column of Fig. 8.

It should be emphasized that both non-depletion approximation analysis and plane-wave analysis results are completely consistent with our simulation and experimental results, which are of great significance for understanding the physics behind the collapsing behaviors of the polarization-structured optical fields in the optically anisotropic nonlinear media.

Finally, we briefly discuss the case when the propagation of light is not along $0°$ or $90°$ with respect to the optic axis of the uniaxial crystal. As is well known, in this case there is the walk-off effect, which will result in the spatial separation of the $o$- and $e$-polarized light. However, this case is relatively complicated, which is beyond the scope of this paper. If the walk-off effect is remarkable, the $o$- and $e$-polarized light may exhibit the large spatial separation, the coupling between them becomes very weak, leading to the fact that the $o$- and $e$-polarized light produces the filaments respectively to form two separate groups of filaments.

## 6. Conclusion

To realize the controllable field collapsing, the crucial problem is able to actively break the symmetry of light-matter interaction and to suppress the random noise simultaneously. We present an idea to actively control the optical field collapsing based on the symmetry broken by the synergy of optical anisotropy and polarization spatial structure. The simulated and experimental results demonstrate that our idea is indeed a very effective method for controlling the optical field collapsing and has the robust feature against random noise.

In experiment, we explore the novel collapsing behaviors of the femtosecond AV-LP-VOFs in MgO:LiNbO$_3$ with both linear anisotropy ($N = n_o^0/n_e^0 > 1$) and nonlinear anisotropy ($\beta < 1/3$); the results show that the $m$-charged AV-LP-VOF produces $2m$ filaments located at azimuthal positions of $\phi(n) = n\pi/m - \delta_0/m$ (where $n = 0, 1, ..., 2m - 1$). In addition, we also explore the collapsing behaviors of the femtosecond AV-LP-VOFs in BaF$_2$ with the linear isotropy ($N = n_o^0/n_e^0 = 1$) but nonlinear anisotropy ($\beta > 1/3$); the results show that the $m$-charged AV-LP-VOF produces $4m$ filaments located at azimuthal positions of $\phi(n) = (2n+1)\pi/4m - \delta_0/m$ (where $n = 0, 1, ..., 4m - 1$). In particular, we clearly reveal the physics behind the multiple filamentation of AV-LP-VOFs in various nonlinear media, based on the non-depletion approximation analysis and the plane-wave analysis.

Our idea has offered the route to produce the controllable and even robust multiple filamentation in the different nonlinear media, thereby facilitating the future development of additional surprising applications. For example, (i) the dynamic filamention produced by rotating the structured media or optical fields, which provides a way for the realization of the dynamic three-dimensional micro-machining; (ii) fabricating the virtual photonic structures, which will be used to manipulate real time the other beams; (iii) the control of multiple filamentation is also helpful for enhancement of terahertz and white light radiation.

## APPENDIX

## 7. Numerical simulations

In this appendix, we will first give the numerical simulations in details, for the collapsing behaviors of AV-LP-VOFs in an anisotropic nonlinear medium.

All the simulations are carried out based on Beam Propagation Method, which is used to numerically solve Eq. (2) or Eq. (3) to model the collapsing behavior of AV-LP-VOFs in the anisotropic MgO:LiNbO$_3$. We classify into two main cases for the detailed discussion as follows. First, in nonlinear media with linear isotropy ($N = 1$, i.e. $n_o^0 = n_e^0$) but nonlinear anisotropy ($\beta \neq 1/3$). Second, in nonlinear media with linear anisotropy ($N > 1$, i.e. $n_o^0 > n_e^0$) and nonlinear anisotropy ($\beta \neq 1/3$).

We should point out that if the spatial random noise is added for simulation, we keep the random noise has a level of 10% amplitude.

Without loss of generality, for all the simulations in this appendix, we select RP-VOF, which is a special case of AV-LP-VOF with $m = 1$ and $\delta_0 = 0$, as an example. For the linear anisotropy, we consider the negative crystal ($N > 1$, i.e. $n_o^0 > n_e^0$).

### 7.1.    In nonlinear media with linear isotropy but nonlinear anisotropy

In this case, we take $n_o^0 = n_e^0 = 2.24717$ for the linear isotropy and $\chi_{11} = \chi_{33} = 9.79522 \times 10^{-16}$ cm$^2$/W for the nonlinear anisotropy. We classify into three subcases based on the value of $\beta$: (i) $\beta = 1/3$, (ii) $\beta = 0.292 < 1/3$, (iii) $\beta = 0.374 > 1/3$.

For **Subcase–(i)** of $\beta = 1/3$, implying the nonlinear isotropy with $\chi_{11} = \chi_{33} = 9.79522 \times 10^{-16}$ cm$^2$/W and $\chi_{16} = 3.26507 \times 10^{-16}$ cm$^2$/W, the simulation results given by Eq. (3) are shown in first and second columns of Fig. 6. In fact, in this subcase, the nonlinear medium degenerates into an isotropic Kerr medium. Clearly, the ideal RP-VOF always remains the axially symmetric doughnut ring, indicating that the ideal RP-VOF cannot converge to the deterministic multiple filaments; but the collapsing filaments produced by RP-VOF with the random noise have the uncertainty which is dominated by the initial random symmetry breaking, similar to the collapses of optical vortices and polarization vortices. In fact, any ideal AV-LP-VOF also remains the axially symmetric doughnut ring but cannot converge to the deterministic multiple filaments; the collapsing filaments produced by AV-LP-VOF with the random noise have the uncertainty.

For **Subcase–(ii)** of $\beta = 0.292 < 1/3$, implying $\chi_{11} = \chi_{33} = 9.79522 \times 10^{-16}$ cm$^2$/W and $\chi_{16} = 2.86026 \times 10^{-16}$ cm$^2$/W for the simulation, these parameters are in fact the practical nonlinear susceptibilities of MgO:LiNbO$_3$. The simulation results given by Eq. (3) are shown in the third and fourth columns of Fig. 6. RP-VOF collapses into four deterministic filaments located at the azimuthal locations of $\phi = 0, \pi/2, \pi, 3\pi/2$. For AV-LP-VOF with $m$ and $\delta_0$, it will collapse into $4m$ deterministic filaments exhibiting the $C_{4m}$ rotation symmetry, located at the azimuthal locations of $\phi(n) = n\pi/2m - \delta_0/m$ (where $n = 0, 1, \ldots, 4m - 1$).

For **Subcase–(iii)** of $\beta = 0.374 > 1/3$, we have $\chi_{11} = \chi_{33} = 9.79522 \times 10^{-16}$ cm$^2$/W and $\chi_{16} = 3.66341 \times 10^{-16}$ cm$^2$/W. In fact, BaF$_2$ belongs to such a kind of crystal, although its parameters are different from those above. The simulation results given by Eq. (3) are shown in fifth and sixth columns of Fig. 6. RP-VOF collapses into four deterministic filaments located at the azimuthal locations of $\phi = \pi/4, 3\pi/4, 5\pi/4, 7\pi/4$. For AV-LP-VOF with $m$ and $\delta_0$, it will collapse into $4m$ deterministic filaments exhibiting the $C_{4m}$ rotation symmetry, located at the azimuthal locations of $\phi(n) = (2n + 1)\pi/4m - \delta_0/m$ (where $n = 0, 1, \ldots, 4m - 1$).

To clearly show the evolution of azimuthal-variant polarization states during the collapsing of RP-VOF in the medium with the linear isotropy but the nonlinear anisotropy, we simulate the ellipticity characterized by the Stocks parameter $S_3$, as shown in Fig. 7. Obviously, the ellipticity of the local polarization state has a tendency to increase induced by the coupling between the two orthogonally polarized components in the nonlinear anisotropic media, which exhibits rich polarization states, including linear polarization, right-handed and left-handed elliptical polarization. For RP-VOF, the local polarization states have no change to keep the initial linear polarization at eight special azimuthal locations of $\phi(n) = n\pi/4$ (where $n = 0, 1, \ldots, 7$) not only for the case of $\beta < 1/3$ but also for the case of $\beta > 1/3$. We can deduce that for the general case of AV-LP-VF with $m$ and $\delta_0$, the local polarization states have no change while still keep
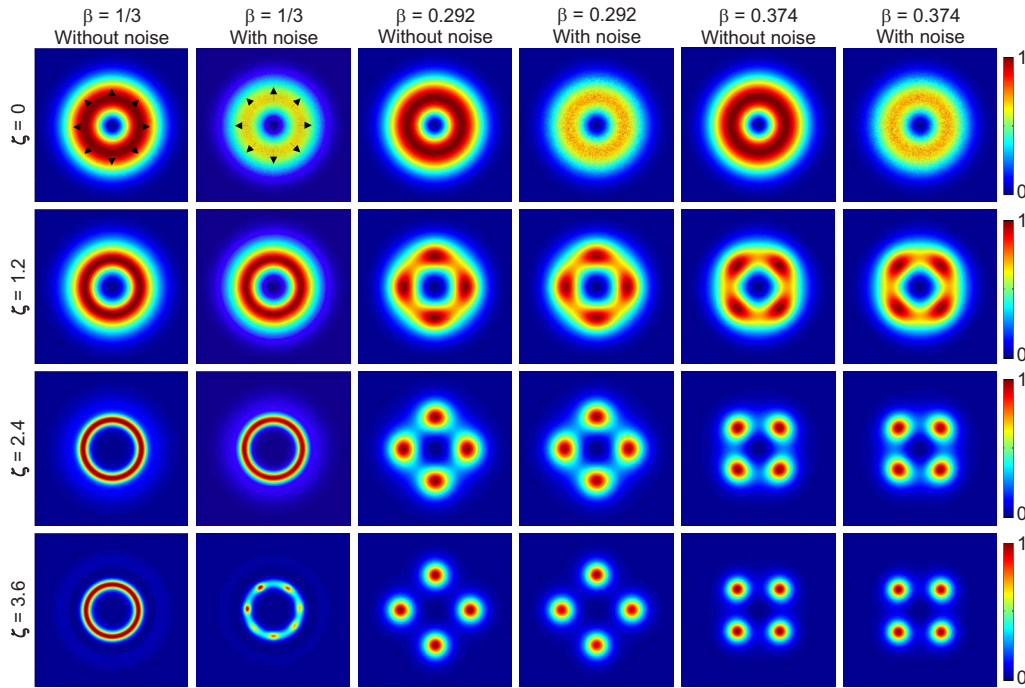
Fig. 6. The simulated collapsing behaviors of RP-VOF (AV-LP-VOF with $m = 1$ and $\delta_0 = 0$) in the nonlinear media with the linear isotropy but the nonlinear anisotropy. For comparison, the first and second columns show the collapsing behavior of RP-VOF in the traditional isotropic Kerr medium.

the initial linear polarization at $8m$ special azimuthal locations of $\phi(n) = n\pi/4m - \delta_0/m$ (where $n = 0, 1, \ldots, 8m - 1$). After comparing Fig. 7 with Fig. 6, we find that the filaments locate at the azimuthal locations, where the local linear polarizations are remained and the ellipticity has a negative slope in both cases of $\beta < 1/3$ and $\beta > 1/3$.

Clearly, the nonlinear anisotropy dominates the collapsing behaviors of AV-LP-VOFs.

### 7.2. In nonlinear media with both linear and nonlinear anisotropies

In this case, we have $n_o^0 = 2.24717$ and $n_e^0 = 2.16539$ for the linear anisotropy, and $\chi_{11} = \chi_{33} = 9.79522 \times 10^{-16}$ cm$^2$/W for the nonlinear anisotropy. We also classify into three subcases: (i) $\beta = 1/3$, (ii) $\beta = 0.292 < 1/3$, (iii) $\beta = 0.374 > 1/3$.

In **Subcase–(i)** of $\beta = 1/3$, i.e. the nonlinear isotropy with $\chi_{11} = \chi_{33} = 9.79522 \times 10^{-16}$ cm$^2$/W and $\chi_{16} = 3.26507 \times 10^{-16}$ cm$^2$/W as well as the linear anisotropy with $n_o^0 = 2.24717$ and $n_e^0 = 2.16539$, the simulation results given by Eq. (2) are shown in the first and second columns of Fig. 8. After comparing with Fig. 6, we find that the self-focusing effect caused by the isotropic nonlinearity makes RP-VOF have a tendency converging to two filaments located at azimuthal locations of $\phi = 0$ and $\pi$. In order to finally achieve two filaments, however, the longer interaction distance in the medium should be needed. This filamentation originates from the axial-symmetry breaking caused by the initial linear anisotropy. The weak linear anisotropy leads to the weak symmetry breaking, therefore, the final filamentation needs the longer nonlinear interaction distance.

In **Subcase–(ii)** of $\beta = 0.292 < 1/3$, we have $n_o^0 = 2.24717$ and $n_e^0 = 2.16539$, $\chi_{11} = \chi_{33} = 9.79522 \times 10^{-16}$ cm$^2$/W and $\chi_{16} = 2.86026 \times 10^{-16}$ cm$^2$/W, all of these are just the practical parameters of the $x$-cut MgO:LiNbO$_3$. The simulation results given by Eq. (2) are shown in
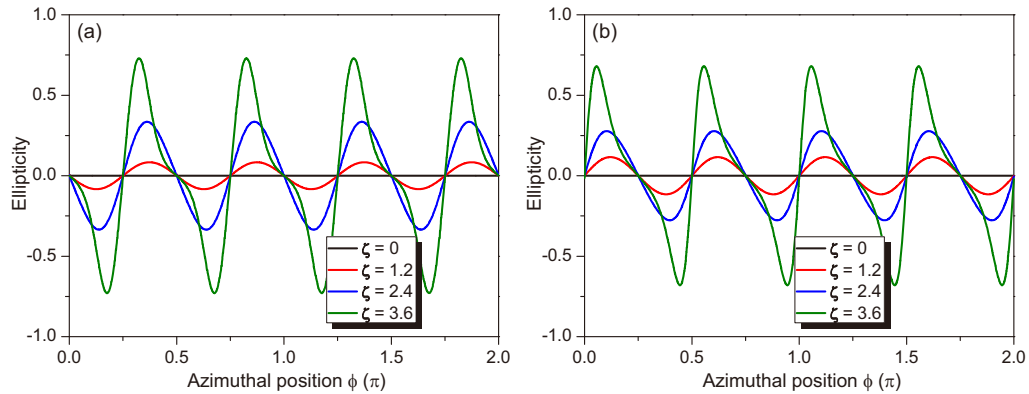
Fig. 7. The simulated evolution $S_3$ of the azimuthal-variant polarization states for RP-VOF (AV-LP-VF with $m = 1$ and $\delta_0 = 0$) in the media with the linear isotropy but the nonlinear anisotropy. (a) $\beta = 0.292 > 1/3$ and (b) $\beta = 0.374 > 1/3$.

the third and fourth columns of Fig. 8. In the initial collapse stage, RP-VOF collapses into four deterministic filaments located at the azimuthal locations of $\phi = 0, \pi/2, \pi$ and $3\pi/2$, which is the same as Fig. 6. However, RP-VOF finally collapses into two deterministic filaments located at the azimuthal locations of $\phi = 0$ and $\pi$, which is in good agreement with the experimental results in Fig. 2 of the main text. This originates from the collaborative contribution of the linear and nonlinear anisotropies to the axial-symmetry breaking. Clearly, the symmetry breaking caused by the linear anisotropy results in that the four filaments of RP-VOF in the linear isotropic nonlinear medium become into the two filaments in the medium with both linear and nonlinear anisotropies. In fact, for AV-LP-VOF with $m$ and $\delta_0$, it will collapse into $2m$ deterministic filaments located at the azimuthal locations of $\phi(n) = n\pi/m - \delta_0/m$ (where $n = 0, 1, \ldots, 2m - 1$).

In **Subcase–(iii)** of $\beta = 0.374 > 1/3$, we have $n_o^0 = 2.24717$ and $n_e^0 = 2.16539$, $\chi_{11} = \chi_{33} = 9.79522 \times 10^{-16}$ cm$^2$/W and $\chi_{16} = 3.66341 \times 10^{-16}$ cm$^2$/W. The simulation results given by Eq. (2) are shown in fifth and sixth columns of Fig. 8. RP-VOF collapses into four deterministic filaments, which are approximately located at the azimuthal locations of $\phi \approx \pi/4, 3\pi/4, 5\pi/4, 7\pi/4$, although they look the same as the fifth and sixth columns of Fig. 6. In fact, the locations of filaments depend on the strength of linear anisotropy (value of $N$), as demonstrated by the simulation result in last column of Fig. 8 (for larger $N = 1.1$) and the analytical result below. For AV-LP-VOF with $m$ and $\delta_0$, it will collapse into $4m$ deterministic filaments, but do not exhibit the $C_{4m}$ rotation symmetry.

## 8. Non-depletion approximation analysis results

We have given the experimental results and the detailed simulation results in various cases. To clearly understand the physics behind the collapse of AV-LP-VOF, the analytic results should be more beneficial. We also classify into two main cases for the detailed discussion.

### 8.1. In nonlinear media with linear isotropy but nonlinear anisotropy

For this case, the analytic discussions are very simple. The discussions in the main text are already enough, so there is no need to repeat them.

### 8.2. In nonlinear media with both linear and nonlinear anisotropies

We discuss the relatively general case when the nonlinear medium has the linear anisotropy ($N > 1$) and the nonlinear anisotropy $\beta \neq 1/3$, simultaneously. To make $\partial\Delta/\partial\phi$ in Eq. (5a), we
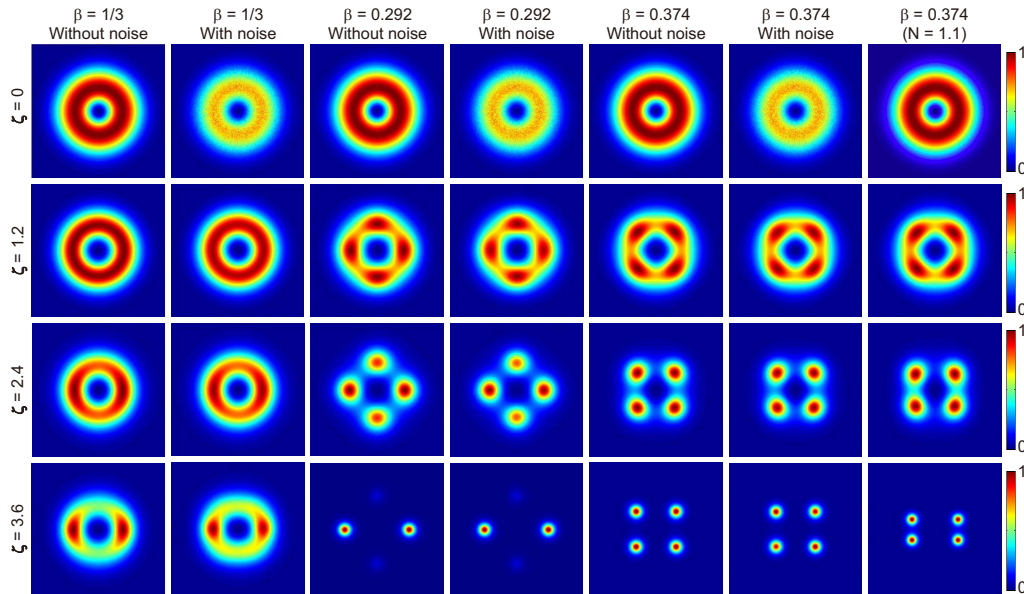
Fig. 8. The simulated collapsing behaviors of RP-VOF (AV-LP-VOF with $m = 1$ and $\delta_0 = 0$) in the media with both the linear and nonlinear anisotropies. For comparison, the first and second columns show the collapsing behaviors of RP-VOF in the media with the linear anisotropy but the nonlinear isotropy $\beta = 1/3$. In particular, the last column shows the collapsing behavior of RP-VOF with the larger linear anisotropy ($N = 1.1$).

require to satisfy Condition-I of $\sin(2\delta) = 0$ or Condition-II of $W = 0$. We can classify into two subcases: Subcase-(i) of $\beta < 1/3$ and Subcase-(ii) of $\beta > 1/3$.

**Subcase–(i)** of $\beta < 1/3$ corresponds to the MgO:LiNbO$_3$ crystal ($V > 0$). Under **Condition-I** of $\sin(2\delta) = 0$, with $\delta = m\phi + \delta_0$, we have $\phi(n) = n\pi/2m - \delta_0/m$ (where $n = 0, 1, ..., 4m - 1$). We will now determine the sign of $\partial^2 \Delta I / \partial \phi^2 \big|_{\sin(2\delta)=0}$ from Eqs. (5) and (6)

$$\frac{\partial^2 \Delta I}{\partial \phi^2}\bigg|_{\sin(2\delta)=0} = \frac{1}{3}m^2 Z^2 \begin{cases} UV, & \text{when} \quad 2\delta = 2n\pi \\ N^2 UV, & \text{when} \quad 2\delta = 2n\pi + \pi \end{cases} \tag{10}$$

Under the Condition-I of $\sin(2\delta) = 0$, due to $U < 0$ and $V > 0$, hence $\partial^2 \Delta I / \partial \phi^2 \big|_{\sin(2\delta)=0} < 0$. Therefore, at the azimuthal locations determined by Condition-I of $\sin(2\delta) = 0$, the filaments can be produced.

**Subcase–(i)** of $\beta < 1/3$ corresponds to the MgO:LiNbO$_3$ crystal ($V > 0$). Under **Condition-II** of $W = 0$, we will now determine the sign of $\partial^2 \Delta I / \partial \phi^2 \big|_{W=0}$ from Eqs. (5) and (6).

$$W = 0$$

$$\Rightarrow UV\cos(2\delta) - (N^2 - 1)\left(U + V\cos^2\delta\right)V\sin^2\delta = 0$$

$$\Rightarrow U\cos(2\delta) = (N^2 - 1)\left(U + V\cos^2\delta\right)\sin^2\delta$$

$$\Rightarrow U - 2U\sin^2\delta = (N^2 - 1)U\sin^2\delta + (N^2 - 1)V\sin^2\delta\cos^2\delta$$

$$\Rightarrow U - 2U\sin^2\delta - (N^2 - 1)U\sin^2\delta = (N^2 - 1)V\sin^2\delta\cos^2\delta$$

$$\Rightarrow U - U\sin^2\delta - N^2U\sin^2\delta = (N^2 - 1)V\sin^2\delta\cos^2\delta$$

$$\Rightarrow U\cos^2\delta - N^2U + N^2U\cos^2\delta = (N^2 - 1)V\sin^2\delta\cos^2\delta$$

$$\Rightarrow U\cos^2\delta + N^2U\cos^2\delta - (N^2 - 1)V\sin^2\delta\cos^2\delta = N^2U$$

$$\Rightarrow \left[(N^2 + 1)U - (N^2 - 1)V\sin^2\delta\right]\cos^2\delta = N^2U$$

$$\Rightarrow -(N^2 - 1)V = U\frac{N^2\sin^2\delta - \cos^2\delta}{\sin^2\delta\cos^2\delta}. \tag{11}$$

$$\frac{\partial W}{\partial\phi} = \frac{\partial}{\partial\phi}\left[UV\cos(2\delta) - (N^2 - 1)\left(U + V\cos^2\delta\right)V\sin^2\delta\right]$$

$$= -2mUV\sin(2\delta) + (N^2 - 1)mV^2\sin(2\delta)\sin^2\delta - (N^2 - 1)m\left(U + V\cos^2\delta\right)V\sin(2\delta)$$

$$= m\left[-2U + (N^2 - 1)V\sin^2\delta - (N^2 - 1)\left(U + V\cos^2\delta\right)\right]V\sin(2\delta)$$

$$= m\left[-2U + (N^2 - 1)V\sin^2\delta - (N^2 - 1)U - (N^2 - 1)V\cos^2\delta\right]V\sin(2\delta)$$

$$= m\left[-(N^2 + 1)U - (N^2 - 1)V\cos(2\delta)\right]V\sin(2\delta). \tag{12}$$

$$\frac{\partial^2\Delta I}{\partial\phi^2}\bigg|_{W=0} = \frac{1}{6}mZ^2\left[\frac{\partial W}{\partial\phi}\sin(2\delta) + 2mW\cos(2\delta)\right]\bigg|_{W=0} = \frac{1}{6}mZ^2\left[\frac{\partial W}{\partial\phi}\sin(2\delta)\right]\bigg|_{W=0}$$

$$= \frac{1}{6}m^2Z^2\left[-(N^2 + 1)U - (N^2 - 1)V\cos(2\delta)\right]V\sin^2(2\delta)$$

$$= \frac{1}{6}m^2Z^2\left[-(N^2 + 1)U + U\frac{N^2\sin^2\delta - \cos^2\delta}{\sin^2\delta\cos^2\delta}\cos(2\delta)\right]V\sin^2(2\delta)$$

$$= \frac{1}{6}m^2Z^2\left[-(N^2 + 1)U + U\frac{N^2\sin^2\delta - \cos^2\delta}{\sin^2\delta\cos^2\delta}\left(\cos^2\delta - \sin^2\delta\right)\right]V\sin^2(2\delta)$$

$$= -\frac{1}{6}m^2Z^2\left[\frac{\cos^2\delta}{\sin^2\delta} + N^2\frac{\sin^2\delta}{\cos^2\delta}\right]UV\sin^2(2\delta). \tag{13}$$

Under the Condition-II of $W = 0$, due to $U < 0$ and $V > 0$, hence $\partial^2\Delta I/\partial\phi^2\big|_{W=0} > 0$. Therefore, in this situation, at the azimuthal locations determined by Condition-II of $W = 0$, the filaments can never be produced.

**Subcase–(ii)** of $\beta > 1/3$ corresponds to $V < 0$. Under **Condition-I** of $\sin(2\delta) = 0$, with $\delta = m\phi + \delta_0$, we have $\phi(n) = n\pi/2m - \delta_0/m$ (where $n = 0, 1, ..., 4m - 1$). We will now determine the sign of $\partial^2\Delta I/\partial\phi^2\big|_{\sin(2\delta)=0}$ from Eqs. (5) and (6). Instead, here we can directly use Eq. (10). Under Condition-I of $\sin(2\delta) = 0$, due to $U < 0$ and $V < 0$, hence $\partial^2\Delta I/\partial\phi^2\big|_{\sin(2\delta)=0} > 0$. Therefore, in this situation, at the azimuthal locations determined by Condition-I of $\sin(2\delta) = 0$, the filaments can never be produced.

**Subcase–(ii)** of $\beta > 1/3$ corresponds to $V < 0$. Under **Condition-I** of $W = 0$, we now determine the sign of $\partial^2 \Delta I / \partial \phi^2 \big|_{\sin(2\delta)=0}$ from Eqs. (5) and (6). Instead, here we can directly use Eq. (13). Under Condition-II of $W = 0$, due to $U < 0$ and $V < 0$, hence $\partial^2 \Delta I / \partial \phi^2 \big|_{\sin(2\delta)=0} < 0$. Therefore, in this situation, at the azimuthal locations determined by Condition-II of $W = 0$, the filaments can be produced.

We will now discuss the dependence of locations of filaments on the linear anisotropy $N$. For Condition-II of $W = 0$, with Eq. (11), we have

$$W = 0 \Rightarrow -(N^2 - 1)V = U \frac{N^2 \sin^2 \delta - \cos^2 \delta}{\sin^2 \delta \cos^2 \delta} \Rightarrow \frac{N^2}{\cos^2 \delta} - \frac{1}{\sin^2 \delta} = \frac{-(N^2 - 1)V}{U}. \tag{14}$$

(A) In the special case of $N \approx 1$ (near linear isotropy), we obtain

$$\frac{1}{\cos^2 \delta} - \frac{1}{\sin^2 \delta} \approx 0.$$

For instance, for RP-VOF with $\delta = \phi$ ($m = 1$ and $\delta_0 = 0$), the filaments will occur at four locations of $\phi \approx \pi/4, 3\pi/4, 5\pi/4, 7\pi/4$.

(B) When the linear anisotropy becomes into larger ($N > 1$), we have

$$\frac{N}{\cos^2 \delta} - \frac{1}{\sin^2 \delta} < 0 \Rightarrow \tan^2 \delta < \frac{1}{N}.$$

For instance, for RP-VOF with $\delta = \phi$ ($m = 1$, $\delta_0 = 0$), the filaments will occur at four locations of $\phi \approx \pi/4 - b, 3\pi/4 + b, 5\pi/4 - b, 7\pi/4 + b$ (where $b$ is a positive constant). This analytic result is in good agreement with the numerical simulation shown in the last column of Fig. 8.

## 9. Plane wave analysis results

Here we will give in detail the plane wave analysis [7–9] for the filamentation of AV-LP-VOF propagation in the nonlinear media.

The steady-state solutions of Eq. (3) can be taken in the form of stationary-wave solutions

$$\psi_o = E_o \exp(j\lambda_o \zeta), \tag{15a}$$

$$\psi_e = E_e \exp(j\lambda_e \zeta), \tag{15b}$$

where $E_o$ and $E_e$ are real and positive functions obeying the differential equations

$$-\lambda_o E_o + \nabla_\perp^2 E_o + B \left[ |E_o|^2 + \beta \left( 2|E_e|^2 + E_e^2 \frac{E_o^*}{E_o} \right) \right] E_o = 0, \tag{16a}$$

$$-\lambda_e E_e + N\nabla_\perp^2 E_e + NB \left[ |E_e|^2 + \beta \left( 2|E_o|^2 + E_o^2 \frac{E_e^*}{E_e} \right) \right] E_e = 0. \tag{16b}$$

Such stationary-wave solutions exist provided that $\lambda_{o,e} > 0$, otherwise $\psi_{o,e}$ and their space derivatives decay to zero at infinity. The first-order perturbation solutions of $\psi_{o,e}$ should be

$$\psi_o = [E_o + \epsilon (\upsilon_o + j\omega_o)] \exp(j\lambda_o \zeta), \tag{17a}$$

$$\psi_e = [E_e + \epsilon (\upsilon_e + j\omega_e)] \exp(j\lambda_e \zeta), \tag{17b}$$

where $\upsilon_{o,e}$ and $\omega_{o,e}$ are real functions, and $\epsilon \ll 1$. By linearizing Eq. (3a) and Eq. (3b), we obtain the problems for $\upsilon_{o,e}$ and $\omega_{o,e}$ as follows

$$\frac{\partial v_o}{\partial \zeta} = L_o^0 \omega_o, \tag{18a}$$

$$\frac{\partial \omega_o}{\partial \zeta} = -L_o^1 v_o + \left[ 2B\beta E_e E_o \left( 2 + \frac{E_o^*}{E_o} \right) \right] v_e, \tag{18b}$$

$$\frac{\partial v_e}{\partial \zeta} = L_e^0 \omega_e, \tag{18c}$$

$$\frac{\partial \omega_e}{\partial \zeta} = -L_e^1 v_e + \left[ 2NB\beta E_o E_e \left( 2 + \frac{E_e^*}{E_e} \right) \right] v_o. \tag{18d}$$

where

$$L_o^0 = \lambda_o - \nabla_\perp^2 - B|E_o|^2 - 2B\beta|E_e|^2 - B\beta E_e^2 \frac{E_o^*}{E_o}, \tag{19a}$$

$$L_e^0 = \lambda_e - N\nabla_\perp^2 - NB|E_e|^2 - 2NB\beta|E_o|^2 - NB\beta E_o^2 \frac{E_e^*}{E_e}, \tag{19b}$$

$$L_o^1 = \lambda_o - \nabla_\perp^2 - 3B|E_o|^2 - 2B\beta|E_e|^2 - B\beta E_e^2 \frac{E_o^*}{E_o}, \tag{19c}$$

$$L_e^1 = \lambda_e - N\nabla_\perp^2 - 3NB|E_e|^2 - 2NB\beta|E_o|^2 - NB\beta E_o^2 \frac{E_e^*}{E_e}. \tag{19d}$$

In the present scope, we are rather interested by the instability of ring-shaped solutions. We define $\bar{\rho}$ as the mean radius of focal field ring, and assume $E_{o,e}$ to be zero everywhere except for in the vicinity of focal field ring. We evaluate the azimuthal-symmetry breaking from Eq. (3) along the path $s = \bar{\rho}\phi$. Thus the Laplacian can be reduced to $\nabla_\perp^2 = \bar{\rho}^{-2}\partial^2/\partial\phi^2$. Under the plane wave analysis, we consider the zeroth-order solutions as

$$\psi_o = E_o \exp\left\{ jB\left[ |E_o|^2 + \beta\left( 2|E_e|^2 + E_e^2 \frac{E_o^*}{E_o} \right) \right] \zeta \right\}, \tag{20a}$$

$$\psi_e = E_e \exp\left\{ jNB\left[ |E_e|^2 + \beta\left( 2|E_o|^2 + E_e^2 \frac{E_e^*}{E_e} \right) \right] \zeta \right\}. \tag{20b}$$

with

$$E_o = N\cos\delta, \tag{21a}$$

$$E_e = \sin\delta, \tag{21b}$$

where $\delta = m\phi + \delta_0$ ($m$ is the topological charge and $\delta_0$ is the initial phase). Azimuthal perturbations take the form of $v, \omega \sim \cos(m\phi)\exp(\gamma_m\zeta)$ and they still obey Eq. (18). We obtain the coupled set of equations

$$\gamma_{m,o}^2 v_o = \frac{m^2}{\bar{\rho}^2}\left( 2B|E_o|^2 - \frac{m^2}{\bar{\rho}^2} \right) v_o + \frac{m^2}{\bar{\rho}^2}\left[ 2B\beta E_e E_o \left( 2 + \frac{E_o^*}{E_o} \right) \right] v_e, \tag{22a}$$

$$\frac{1}{N^2}\gamma_{m,e}^2 v_e = \frac{m^2}{\bar{\rho}^2}\left( 2B|E_e|^2 - \frac{m^2}{\bar{\rho}^2} \right) v_e + \frac{m^2}{\bar{\rho}^2}\left[ 2B\beta E_o E_e \left( 2 + \frac{E_e^*}{E_e} \right) \right] v_o. \tag{22b}$$

In particular, the azimuthal modulational instability (AMI) growth rates for the $o$, $e$ components satisfy $\gamma_{m,o}^2 = \gamma_{m,e}^2/N^2 = \gamma_m^2$ (which originate from a simple argument of symmetry). With the above equations governing $v_o$ and $v_e$, we yield

$$\gamma_m^2 = \frac{m^2}{\bar{\rho}^2}\left( 2\triangle_\pm - \frac{m^2}{\bar{\rho}^2} \right) \tag{23a}$$

with

$$2\triangle_{\pm} = B\left[\left(|E_o|^2 + |E_e|^2\right) \pm \sqrt{\left(|E_o|^2 - |E_e|^2\right)^2 + (2\beta E_o E_e)^2\left(2 + \frac{E_o^*}{E_o}\right)\left(2 + \frac{E_e^*}{E_e}\right)}\right]. \quad (23b)$$

Combination of Eq. (21) and Eq. (23), we can obtain

$$\gamma_m^2 = \frac{m^2}{\bar{\rho}^2}\left\{B\left[\left(N^2\cos^2\delta + \sin^2\delta\right) + \sqrt{\left(N^2\cos^2\delta - \sin^2\delta\right)^2 + N^2(3\beta)^2\sin^2(2\delta)}\right] - \frac{m^2}{\bar{\rho}^2}\right\}. \quad (24)$$

Here we also classify into three subcases: (i) $\beta = 1/3$, (ii) $\beta = 0.292 < 1/3$, (iii) $\beta = 0.374 > 1/3$. Based on Eq. (24), the detailed analytic results of $\gamma_m^2$ have been shown in Fig. 9. It should be pointed out that $\gamma_m^2$ has been normalized by its maximum value. Without loss of generality, we select RP-VOF for discussion. For the linear anisotropy, we consider the negative crystal ($N > 1$). In order to determine the azimuthal locations of filaments, the key is to find the normalized $(\gamma_m^2)_{max}$.
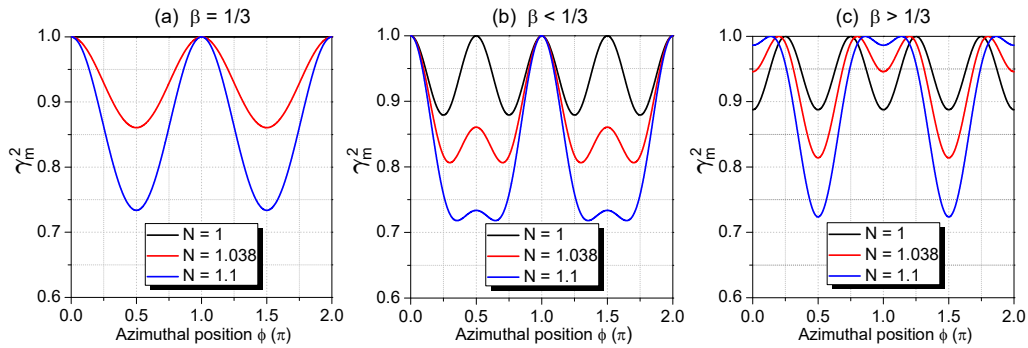


Fig. 9. The normalized AMI growth rate of RP-VOF in different nonlinear media with (a) $N \geq 1$, $\beta = 1/3$; (b) $N \geq 1$, $\beta < 1/3$; (c) $N \geq 1$, $\beta > 1/3$

**Subcase–(i)** of $\beta = 1/3$ is shown in Fig. 9(a). When $N = 1$, this corresponds to the traditional isotropic Kerr nonlinear medium, we have $\gamma_m \equiv 1$, implying that any azimuthal position is equivalent or indistinguishable for any AV-LP-VOF. Therefore, any purely ideal AV-LP-VOF can never produce the deterministic multiple filamentation. However, when $N > 1$, $(\gamma_m^2)_{max}$ of RP-VOF are located at $\phi = 0$ and $\pi$, which originates from the axial-symmetry breaking caused by the initial linear anisotropy.

**Subcase–(ii)** of $\beta < 1/3$ is shown in Fig. 9(b). When $N = 1$, $(\gamma_m^2)_{max}$ of RP-VOF are located at four azimuthal locations of $\phi = 0$, $\pi/2$, $\pi$ and $3\pi/2$, which are owing to the nonlinear anisotropy ($\beta < 1/3$). However, when $N > 1$, $(\gamma_m^2)_{max}$ of RP-VOF are located at two azimuthal locations of $\phi = 0$ and $\pi$, which originate from the collaborative contribution of the linear and nonlinear anisotropies to the axial-symmetry breaking. Clearly, the symmetry breaking caused by the linear anisotropy ($N > 1$) results in that four $(\gamma_m^2)_{max}$ of RP-VOF in the linear isotropic nonlinear medium become into two $(\gamma_m^2)_{max}$ in both linear and nonlinear anisotropic medium. In fact, AV-LP-VOF will collapse into $2m$ deterministic filaments located at azimuthal locations of $\phi(n) = n\pi/m - \delta_0/m$ (where $n = 0, 1, ..., 2m - 1$), which are in completely agreement with both the experimental results in the MgO:LiNbO$_3$ crystal, the simulation results and the non-depletion approximation analysis results.

**Subcase–(iii)** of $\beta > 1/3$ is shown in Fig. 9(c), when $N = 1$, this corresponds to the BaF$_2$ crystal, $(\gamma_m^2)_{max}$ located at four azimuthal locations of $\phi = \pi/4$, $3\pi/4$, $5\pi/4$, $7\pi/4$, which are

corresponding to the four deterministic filaments; when $N > 1$, $(\gamma_m^2)_{\max}$ of RP-VOF will also determine four filaments in the medium ($N = 1.038$, $\beta > 1/3$), which are approximately located at the azimuthal locations of $\phi \approx \pi/4 - b, 3\pi/4 + b, 5\pi/4 - b, 7\pi/4 + b$ (where $b$ is a positive constant, and $b$ becomes larger as $N$ increases). In other words, the locations of filaments depend on the strength of linear anisotropy (the value of $N$), as demonstrated by the analytical result of the case (for lager $N = 1.1$) are in good agreement with the numerical simulation shown in the last column of Fig. 8.

## Funding

## Acknowledgments